

1     **A Model Investigation of Aerosol-induced Changes in Boreal**  
2                     **Winter Extratropical Circulation**

3                     YI MING <sup>\*</sup> AND V. RAMASWAMY

*Geophysical Fluid Dynamics Laboratory/NOAA, Princeton, NJ*

4                     GANG CHEN

*Department of Earth and Atmospheric Sciences, Cornell University, Ithaca, NY*

---

<sup>\*</sup> *Corresponding author address:* Yi Ming, Geophysical Fluid Dynamics Laboratory/NOAA, P. O. Box 308, Princeton, NJ 08542.

E-mail: Yi.Ming@noaa.gov

## ABSTRACT

We examine the key characteristics of the boreal winter extratropical circulation changes in response to anthropogenic aerosols, simulated with a coupled atmosphere-slab ocean general circulation model. The zonal-mean response features a pronounced equatorward shift of the Northern Hemisphere subtropical jet owing to the mid-latitude aerosol cooling. The circulation changes also show strong zonal asymmetry. In particular, the cooling is more concentrated over the North Pacific than over the North Atlantic despite similar regional forcings. With the help of an idealized model, we demonstrate that the zonally asymmetrical response is linked tightly to the stationary Rossby waves excited by the anomalous diabatic heating over the tropical East Pacific. The altered wave pattern leads to a southeastward shift of the Aleutian low (and associated changes in winds and precipitation), while leaving the North Atlantic circulation relatively unchanged.

Despite the rich circulation changes, the variations in the extratropical meridional latent heat transport are controlled strongly by the dependence of atmospheric moisture content on temperature. This suggests that one can project reliably the changes in extratropical zonal-mean precipitation solely from the global-mean temperature change, even without a good knowledge of the detailed circulation changes caused by aerosols. On the other hand, such knowledge is indispensable for understanding zonally asymmetrical (regional) precipitation changes.

# 1. Introduction

The Earth’s climate system is comprised of distinct regimes, depending mainly on latitude and season. When one moves from the tropics into the wintertime extratropics, stationary Rossby waves and baroclinic eddies overtake the time-mean flow as the main mechanism of poleward energy and moisture transport. In light of the fundamental differences between the two climate regimes, we use this paper to examine specifically the impacts of aerosols on the boreal winter extratropical circulation. The other two papers in the present series focus mainly on the tropical and monsoon circulations, respectively (Ming and Ramaswamy 2011; Ming et al. 2011a).

The general circulation model (GCM)-simulated climate response to global warming was studied extensively (e.g., Hall et al. 1994; Kushner et al. 2001; Yin 2005; Lu et al. 2007; Lorenz and DeWeaver 2007). More specifically, Hall et al. (1994) and Yin (2005) examined the changes in the characteristics of storm tracks, while Lu et al. (2007) focused on the Hadley circulation. Kushner et al. (2001) studied how the warming may affect the Southern Hemisphere (SH) extratropical circulation and Southern Annular Mode. Lorenz and DeWeaver (2007) used a simple dry GCM to explore the influence of an increase in tropopause height on the mid-latitude circulation. A much discussed phenomenon was the poleward displacement of the subtropical jet streams and storm tracks, accompanied by an expansion of the Hadley circulation. This has been linked to increased subtropical static stability (e.g., Frierson et al. 2007; Lu et al. 2008), to stronger meridional temperature gradients near the tropopause as a result of concurrent tropical upper tropospheric warming and stratospheric cooling (e.g., Chen and Held 2007; Chen et al. 2008), and to a higher tropopause (Lorenz and DeWeaver

2007). A few studies (e.g., Krisjánsson et al. 2005; Ming and Ramaswamy 2009) identified an equatorward shift of storm tracks as part of the response to aerosol cooling. This result is in qualitative agreement with the past work on a similar shift in the cold climate during the last glacial maximum (LGM) (Williams and Bryan 2006; Toggweiler et al. 2006). One may be tempted to draw the conclusion that both the warming and cooling cases are governed by the same mechanism, and the direction of the shift depends only on the sign of temperature change. Consistent with this line of thinking, Fischer-Bruns et al. (2009) argued that aerosol cooling merely offsets the warming-induced poleward shift by lessening the decrease in baroclinicity. In this paper, we try to shed more light on this specific issue.

It is useful to think of aerosol impacts on the extratropics in terms of physical mechanisms. Aerosols are abundant in the Northern Hemisphere (NH) mid-latitudes, where the major industrial regions lie. By scattering and/or absorbing insolation (either directly or through altering clouds), they pose *direct* thermal forcing on circulation. Ming and Ramaswamy (2011) and Ming et al. (2011a) showed the richness of the tropical response to aerosols. It is well known that a change in the tropical state can influence the extratropical climate. There is a large body of work that documented the crucial role of stationary Rossby waves in establishing the teleconnection between the tropics and extratropics (e.g., Lau 1997; Alexander et al. 2002). It is intriguing to see how these tropical variations would project onto the extratropics by exciting planetary waves. In this context, aerosol impacts are initiated *indirectly*. This study explores the validity of this paradigm.

Some details helpful for understanding the results are provided here. Ming and Ramaswamy (2009) described the atmospheric GCM (AGCM) and its coupling with a slab (mixed-layer) ocean model, and the design of the experiments examined in this study. The

AGCM is based on the Geophysical Fluid Dynamics Laboratory (GFDL) AM2.1 model (The GFDL Global Atmospheric Model Development Team 2004), but modified to include a prognostic treatment of aerosol indirect effects (Ming et al. 2006, 2007). The climatological atmospheric burdens of sulfate, black carbon, organic carbon and dust are generated by running a chemical transport model (Horowitz 2006), and thus do not interact with the GCM-simulated meteorology and climate. Sea salt within the marine boundary layer is parameterized as a function of satellite-retrieved surface wind speed (Haywood et al. 1999).

With all the climate forcings set at their 1860 values, the pre-industrial control (CONT) simulation lasts 140 model years. Three perturbation cases are created from subjecting the control at the beginning of Year 41 to present-day aerosols (AERO), to present-day radiatively active gases (GAS), and to aerosols and gases simultaneously (BOTH). Note that the term “present-day” refers specifically to 1990 in this study. After reaching equilibrium after  $\sim 20$  model years, each of the perturbation experiments is integrated for another 80 model years. The equilibrium responses and their statistical significance are computed from the last 80 years of the simulations.

The combined aerosol direct (by scattering/absorbing sunlight) and indirect (by altering cloud properties) effects can be quantified as a radiative flux perturbation, which is the variation in the top-of-the-atmosphere radiative flux after the atmosphere adjusts to the presence of a climate forcing agent (Hansen et al. 2005; Haywood et al. 2009). In this model, the pre-industrial to present-day increases of anthropogenic aerosols give rise to a global-mean radiative flux perturbation of  $-2.1 \text{ W m}^{-2}$ , about 74% of which is due to indirect effects. The geographical distribution is highly inhomogeneous, with some of the strongest forcing over the NH mid-latitude source regions (e.g., East Asia, North America

and Europe) and over the oceans downwind of them (e.g., North Pacific and North Atlantic) (Fig. 1). The tropical aerosol forcing caused mainly by biomass burning is centered over the sources (e.g., Central Africa, Amazon, South Asia and Southeast Asia). In comparison, the instantaneous radiative forcing and radiative flux perturbation of radiatively active gases are 2.5 and 2.1 W m<sup>-2</sup>, respectively. Despite the relatively small difference between them due to the atmospheric-only adjustment to gases, both forcing measures are distributed rather evenly over the entire globe.

We first discuss the changes in the boreal winter (December - February) extratropical zonal-mean and zonally asymmetrical flows (stationary eddies) caused by aerosols and gases (BOTH), while attributing them to specific forcing by comparing with the individual responses (AERO and GAS). Then, we examine how the altered time-mean flow may affect the transient eddy activity, and the meridional transport of moist static energy and moisture.

## 2. Zonal-mean Flow

The zonal-mean change in potential temperature ( $\theta$ ) due to aerosols and gases (BOTH) is plotted in Fig. 2(a). Some of the characteristics (e.g., enhanced warming in the tropical upper troposphere, polar amplification of warming and stratospheric cooling) are clearly associated with GAS (Fig. 2(c)). Even though the negative aerosol forcing far outweighs the positive gas forcing over the NH mid-latitude aerosol source regions (Fig. 1), the combined effect is only a mild surface cooling of a few tenths of a degree, hinting at mitigation of aerosol cooling by circulation adjustment. In the mid-latitude troposphere, the cooling decreases gradually with altitude below  $\sim 400$  hPa, while the gas-induced warming dominates above.

This results in a decrease in lapse rate ( $\Gamma$ ) and an increase in dry static stability. In contrast, the cooling is amplified in the upper troposphere in response to aerosols alone (AERO) (Fig. 2(b)). As discussed in Section 6, the stabilizing effect of gases outweighs the destabilization effect of aerosols.

The poleward shift of the SH subtropical jet and the equatorward shift of its NH counterpart are pronounced in Fig. 3(a), which depicts the change in zonal wind ( $u$ ) in BOTH. They are of different origins. The former is attributed to the gas-induced warming (Fig. 3(c)) (e.g., Hall et al. 1994; Kushner et al. 2001; Yin 2005). As shown in Figs. 2(a) and 2(b), the aerosol-induced cooling collocates approximately with the mean location of the NH jet. It strengthens the meridional temperature gradient on the equatorward side of the jet, while weakening it on the poleward side. According to the thermal wind relationship, the westerlies accelerate in the former case, and decelerate in the latter, giving rise to a net equatorward displacement of the jet (Figs. 3(a) and 3(b)). This indicates that the local aerosol forcing is capable of reversing the warming-induced poleward shift. The surface winds display a similar equatorward shift that cannot be explained by the thermal wind (not shown); it has to be related to the change in eddy momentum flux and associated mean meridional circulation. Note that this result does not agree with the observed poleward expansion of the Hadley circulation in both hemispheres (e.g., Fu et al. 2006; Hu and Fu 2007). The reasons are manifold. The equilibrium climate response discussed here by definition has not been fully realized in the real world. As aerosol forcing suffers from large uncertainties (e.g., Forster et al. 2007), its magnitude and impact on the location of the NH subtropical jet may have been exaggerated in this study. Moreover, climate models generally have difficulties in capturing the full extent of the observed expansion (Johanson and Fu 2009). The model

used here may have the same deficiency.

By computing the lapse rate linearly with pressure between model layers (Reichler et al. 2003), we estimate the tropopause height from the vertical temperature profile as the lowest pressure level at which the lapse rate drops below  $2 \text{ K km}^{-1}$  (World Meteorological Organization (WMO) 1957). The tropopause rises almost uniformly by 3 - 4 hPa between  $30^\circ\text{S}$  and  $30^\circ\text{N}$  in BOTH (Fig. 4). The rise is even greater (more than 10 hPa) in the SH extratropics, thus lessening the downward slope of the tropopause. In contrast, the NH extratropical tropopause generally rises only by  $\sim 2$  hPa, leaving the local slope little changed. One can understand the different hemispheric responses from the individual responses simulated in AERO and GAS. For aerosols, the lowering of the troposphere occurs at all the latitudes, but is more pronounced in the extratropics than in the tropics. The precipitous drop at  $\sim 40^\circ\text{N}$  coincides with the equatorward shift of the NH subtropical jet, as the jet roughly divides the tropics (with higher tropopause) and extratropics. Conversely, the poleward shift of the subtropical jets associated with warming has a tendency of elevating the tropopause in both hemispheres. It is clear from Fig. 4 that the two opposite effects are roughly linear in the tropics, but not so in the extratropics (especially in the NH extratropics), an important point to which we shall return in Section 6. They largely offset each other in the tropics and NH extratropics, while the gas effect dominates in the SH extratropics.

### 3. Zonally Asymmetrical Flow

The longitudinal variations in the Earth's climate arise from zonally asymmetrical boundary conditions such as topography and the land-sea contrast in diabatic heating, which are



capable of exciting stationary Rossby waves (Held et al. 2002). From the viewpoint of climate change, a change in diabatic heating can alter stationary wave patterns, and thus affect regional climate. Another potential source of zonal asymmetry in the context of climate change is inhomogeneous forcing. This is particularly true of aerosols. These two factors are often intertwined, and may not be separated cleanly.

The change in surface temperature ( $T_s$ ) caused by aerosols and gases has rich spatial structures (Fig. 5(a)). The aerosol cooling occurs mostly in the NH mid-latitudes, but varies within the latitudinal band. Of particular interest is that the cooling appears to organize tightly into an elongated region approximately along the North Pacific storm track, but is much more scattered over the North Atlantic, despite similar distributions of aerosol forcing over two oceans (Fig. 1). This pattern is also present in AERO (Fig. 5(b)). (We will discuss the cause of this distinction later in this section.) This explains why the equatorward shift of the NH subtropical jet seen in the zonal-mean flow takes place preferentially over the North Pacific (Figs. 6(a) and 6(b)). Besides, the strong warming over parts of northernmost Eurasia and North America lies immediately north of the North Pacific cooling, giving rise to a substantial reduction in the local meridional temperature gradient, and further decelerating the poleward flank of the jet. In contrast, the SH extratropical warming and accompanying poleward shift of the jet in BOTH are fairly uniform across the latitudinal band (Figs. 5(a) and 6(a)), consistent with GAS (Figs. 5(c) and 6(c)). Note that the tropical Pacific warming in BOTH is El Niño-like (i.e., the warming over the East Pacific is greater than over the West Pacific), a pattern common to the GCM-simulated response to global warming (Vecchi et al. 2008).

The lower pressure over the entire extratropical North Pacific is characteristic of the

change in sea level pressure (SLP) caused by aerosols and gases, and constitutes a south-eastward shift of the Aleutian low (Fig. 7(a)). This is in sharp contrast with the generally higher pressure over the North Atlantic - European sector. These circulation changes are barotropic as they are also present over the same regions in the changes in 500-hPa geopotential height ( $Z$ ) (Fig. 8(a)) and in 300-hPa stationary eddy stream function ( $\Psi$ ) (Fig. 9(a)). A comparison with the individual responses (Panels (b) and (c) in Figs. 7 - 9) yields that these characteristics are broadly consistent with AERO, instead of GAS, indicating that they are attributable to anthropogenic aerosols. Note that the pattern of a trough over the North Pacific and a ridge over North America in the combined response resembles the classical Pacific - North America (PNA) teleconnection response to El Niño (see Fig. 2(a) of Lau 1997). In light of the El Niño-like tropical Pacific warming as discussed above, it is tempting to contemplate the link between the East Pacific oceanic state and the extratropical circulation.

An observation is that the change in the stationary eddy stream function is wave-like (Fig. 9(a)). (This is not nearly as evident for  $Z$ , particularly in the tropics, as  $Z \propto f\Psi$ .  $f$  is the Coriolis parameter.) Note that zonally asymmetrical diabatic heating is a main source of stationary Rossby waves (Held et al. 2002). Fig. 10(a) shows the change in precipitation ( $P$ ), which can be viewed roughly as a proxy for diabatic heating, in response to aerosols and gases. It features a substantial reduction in precipitation north of the equator and an increase of comparable magnitude to the south. Because this overall pattern resembles that of AERO (Fig. 10(b)), but is missing from GAS (Fig. 10(c)), one can attribute it to the former. In fact, this southward shift of rainfall is a reasonably robust hydrological response to aerosols across different models (Williams et al. 2001; Rotstayn and Lohmann 2002; Feichter

et al. 2004; Krisjánsson et al. 2005). As explained in Ming and Ramaswamy (2011), the tropical circulation adjustment to aerosols is driven fundamentally by the need to lessen the energy imbalance between NH and SH. Although the change in rainfall implies more latent energy being transported from NH to SH, this effect is not strong enough to reverse the enhanced export of dry static energy in the opposite direction. The net northward cross-equatorial moist static energy flux compensates for the radiative deficit posed by aerosols in the NH (see Section 5). In the extratropics, the precipitation associated with the North Pacific storm track shows a southeastward shift, consistent with the change in SLP (Fig. 7(a)). One wonders how the change in diabatic heating, with its complex spatial structures, would affect wave pattern and circulation.

We answer this question with a set of idealized model experiments, which are described in the Appendix. It is reassuring to see that the idealized model, when being forced by the GCM-simulated diabatic heating in CONT or in BOTH, can capture reasonably well the main characteristics of the stationary eddy climatology and the response to the difference in heating simulated with the full GCM (Fig. 11(a)). An example is the PNA pattern discussed above. This demonstrates the model’s utility for interpreting the full GCM simulations. We are able to decompose the total response into those forced by the differences in diabatic heating over three regions, namely the tropical Indian Ocean and West Pacific (30°S - 30°N and 0° - 150°E), the tropical East Pacific and Atlantic (30°S - 30°N and 150°E - 0°) and the extratropical North Pacific and North Atlantic (north of 30°N) (Figs. 11(b) - (d)). Note that the simulated total response (Fig. 11(a)) is grossly similar to the linear sum of the three individual responses (Fig. 11(e)).

In Fig. 11(b), a wave train emanates from the tropical Indian Ocean and West Pacific into

the NH mid-latitudes. It then turns around over the North Pole, with the tilt changing from northwest (NW)-southeast (SE) to northeast (NE)-southwest (SW), before being absorbed by the tropics over the Pacific. A cyclone forms over the North Pacific ( $\sim 30^\circ - 60^\circ\text{N}$ ) along with an anticyclone to its southeast over the tropical Pacific ( $\sim 15^\circ - 30^\circ\text{N}$ ). The wave source over the tropical East Pacific is evident in Fig. 11(c). The northward propagation with NW-SE tilt is associated with a cyclone centered at  $\sim 30^\circ\text{N}$  over the Pacific and a pronounced anticyclone over North America, which constitute a PNA-like pattern. The extratropical heating excites a wave train with NE-SW tilt, leading to a cyclone approximately at  $30^\circ - 50^\circ\text{N}$  over the North Pacific (Fig. 11(d)). Thus, we conclude that the mid-latitude circulation change is driven mainly by the heating anomaly over the tropical East Pacific, as opposed to that over the tropical Indian Ocean and West Pacific. This finding is consistent with the previous studies of the influence of El Niño on the extratropical circulation (e.g., Lau 1997). Despite this apparent similarity, one has to note that the wave train is typically forced by a longitudinal shift of heating from the West Pacific to the East Pacific in a real El Niño event. Here, when all the heating sources are considered, the shift is mainly in the latitudinal direction. The latter shift is more symmetrical in the zonal direction than the former, and thus is less efficient at exciting stationary Rossby waves.

We return to the question of why the spatial distributions of the temperature change are so different over the two oceans: the aerosol-induced cooling is much more concentrated over the North Pacific between  $\sim 30^\circ - 60^\circ\text{N}$  than over the North Atlantic. As discussed above, the change in tropical diabatic heating modulates strongly the time-mean flow over the North Pacific by exciting stationary Rossby waves, while leaving the North Atlantic largely unaffected. The large change in the zonal wind over the North Pacific can be achieved

only by maintaining strong local meridional temperature gradients. This is an important contributing factor to the zonally asymmetrical climate response.

## 4. Transient Eddies

As an effective means of transporting energy and momentum, baroclinic eddies play important roles in driving the general circulation and hydrological cycle. In response to aerosols and gases, a substantial reduction in 300-hPa transient eddy kinetic energy occurs over the North Pacific, and extends downstream into North America (Fig. 12(a)). The less energetic eddies and lower temperature (less moisture) (Fig. 5(a)) contribute to a suppression of precipitation on the poleward side of the Pacific storm track (Fig. 10(a)). One can relate the production of baroclinic eddies to the state of the time-mean flow with the maximum Eady growth rate ( $\sigma_{BI}$ ) (Lindzen and Farrell 1980; Hoskins and Valdes 1990). It is defined as  $0.31(f/N)|\partial \mathbf{v}/\partial z|$ , where  $N$  is the Brunt-Väisälä frequency,  $\mathbf{v}$  is the horizontal wind vector and  $z$  is the geometric height.  $\sigma_{BI}$  at 500 hPa shows a pronounced decrease over the North Pacific (Fig. 13(a)), a pattern broadly consistent with the difference in eddy kinetic energy. A further analysis indicates that  $\delta\sigma_{BI}$  arises mainly from the change in vertical wind shear, which is tied to the change in the local meridional temperature gradient caused by the concentrated aerosol cooling (Fig. 5(a)), while the dry static stability, and thus  $N$  are little changed in the middle troposphere (Fig. 2). This argument is consistent with the fact that weaker transient eddies and slower Eady growth rates also take place in AERO, but not in GAS (Panels (b) and (c) in Figs. 12 - 13)). Lorenz and DeWeaver (2007) reported large increases in the annual average zonal-mean eddy kinetic energy on the poleward sides of the

storm tracks owing to strong CO<sub>2</sub>-induced warming. That finding does not contradict the aerosol effects discussed here.

## 5. Atmospheric Moist Static Energy Transport

One may attempt to understand the collective climate impacts of the detailed circulation changes by examining the variations in the atmospheric transport of energy and moisture. As explained in Ming and Ramaswamy (2011), the interhemispheric asymmetry in aerosol forcing leads to a net cross-equatorial moist static energy flux from SH to NH through strengthening the boreal winter Hadley circulation (Fig. 14(b)). This supply of energy is deposited mainly between 0° - 60°N, where most aerosol forcing is located. A cross-equatorial flux of similar magnitude is also present in BOTH (Fig. 14(a)), suggesting that this phenomenon has its root in the aerosol-induced tropical circulation adjustment. As shown in Fig. 15, the overall shape of the change in the total atmospheric energy transport ( $\delta F$ ) is similar to that of the linear sum of the individual responses.

Because of the strong dependence of the saturated water vapor pressure on temperature (the Clausius-Clapeyron scaling), the warming-induced change in latent heat transport ( $\delta F_L$ ) is thermodynamically controlled to the first order (i.e., proportional to  $\delta T_s$ ) (Held and Soden 2006). To test to what extent this argument holds for aerosols, we estimate  $\delta F_L$  for AERO or BOTH by scaling the actual  $\delta F_L$  for GAS with the global-mean  $\delta T_s$  in each case. For example,  $\delta F_{L,AERO}$  can be calculated as  $\delta F_{L,GAS} \delta T_{s,AERO} / \delta T_{s,GAS}$ . The agreement between the simulated and estimated  $\delta F_L$  is excellent in the extratropics, indicating that it is still valid to assume the thermodynamic control of  $\delta F_L$ . The results are somewhat surprising given

that aerosols are rather potent at altering regional circulations, and once again reminds one how strongly the Clausius-Clapeyron scaling controls the hydrological response.

The changes in latent heat and dry static energy transport ( $\delta F_D$ ) in response to global warming are often of opposite signs (e.g., Manabe and Wetherald 1975; Held and Soden 2006). This is true not only for GAS (Fig. 14(c)), but also for AERO (Fig. 14(b)). The difference is that decreased  $F_D$  cancels out part of increased  $F_L$  in the extratropics in the former case, while decreased  $F_L$  compensates for a large fraction of increased  $F_D$  in the latter. For BOTH,  $F_L$  is almost negligible north of  $\sim 40^\circ\text{N}$  as a result of small temperature change. The increase in atmospheric energy transport is realized mainly by enhanced  $F_D$ . It would be of interest to investigate whether these characteristics specific to aerosols are present in fully coupled atmosphere-ocean general circulation models (AOGCM) in light of the potentially important role of oceanic energy transport (Held and Soden 2006).

## 6. Nonlinear Thermal Response

The simulated surface temperature change in response to aerosols and gases deviates from the linear sum of the individual responses in NH (Fig. 16), an issue highlighted in Ming and Ramaswamy (2009). Particularly intriguing is the small yet robust nonlinearity in the low and mid-latitudes, where the surface albedo feedback is absent, and thus can be ruled out as cause of the nonlinearity. It is also reflected in the change in 300-hPa zonal-mean  $u$  (Fig. 17). The NH subtropical jet undergoes a distinct equatorward shift in AERO, while moving poleward in GAS. The linear sum of AERO and GAS captures the overall pattern of wind change in BOTH (i.e., an equatorward displacement that is less pronounced than in AERO),

312 but significantly underestimates the acceleration on the equatorward flank of the jet.

313 One can relate the mean location of the jet to baroclinic instability ( $C$ ) using the Phillips  
314 (1954) criterion, which states  $C \propto u_z/\theta_z$  with  $u_z = u_{500} - u_{850}$  and  $\theta_z = \theta_{500} - \theta_{850}$ . The  
315 subscripts denote the pressure levels (in hPa) at which  $u$  and  $\theta$  are evaluated. Lu et al.  
316 (2008) utilized this criterion to study the poleward jet shift and expansion of the Hadley  
317 circulation associated with global warming. The changes in  $u_z$  and  $\theta_z$  between  $10^\circ - 35^\circ\text{N}$ ,  
318 where the eddy momentum flux divergence is crucial for forming the descending branch of  
319 the Hadley circulation, are listed in Table 1. The warming caused by gases decreases slightly  
320 the vertical wind shear, while having a strong stabilizing effect on the thermal structure  
321 of the troposphere (i.e., weaker  $\Gamma$ ) owing to moist convective adjustment and increased  
322 longwave absorption. In contrast, the aerosol cooling leads to a substantial increase in wind  
323 shear as a result of stronger meridional temperature gradients, and a small decrease in dry  
324 static stability. A comparison of BOTH with the linear sum of AERO and GAS suggests  
325 that  $\delta\theta_z$  is approximately linear, but  $\delta u_z$  behaves nonlinearly. Since  $\delta u_z$  is approximately  
326 proportional to the meridional temperature gradient (i.e., the thermal wind relationship),  
327 the nonlinearity in  $\delta u_z$  is consistent with the nonlinear thermal response discussed above.  
328 Because  $\delta C/C = \delta u_z/u_z - \delta\theta_z/\theta_z$ , the effects of  $\delta u_z$  and  $\delta\theta_z$  on  $C$  can be separated in terms  
329 of fractional changes (Table 1). Aerosols increase baroclinic instability mainly by enhancing  
330 wind shear, thus causing the tropical poleward flow to descend at a lower latitude and an  
331 equatorward shift of the jet, while gases decrease it mainly by stabilizing the troposphere,  
332 thus resulting in a poleward shift. If  $\delta u_z$  and  $\delta\theta_z$  both behave linearly, the two opposite  
333 effects would largely cancel out, and leave the location of the jet unchanged, an outcome  
334 that obviously does not materialize in BOTH. Instead, the simulated meridional temperature



gradient is stronger than suggested by the linear sum. The resulting net increase in baroclinic instability is consistent with the simulated equatorward shift of the jet. Note that the above argument is framed in the context of subtropical static stability and baroclinic instability (e.g., Frierson et al. 2007; Lu et al. 2008). It could be beneficial to approach the same issue from other angles such as near-tropopause meridional temperature gradient (e.g., Chen and Held 2007; Chen et al. 2008).

An inspection of the change in tropopause height (Fig. 4) yields a clue to the root cause of the nonlinearity. The linear sum indicates that the equatorward flank of the NH jet would move poleward (as the gas effect dominates locally), while the poleward flank would move in the opposite direction (i.e., equatorward) owing to the aerosol effect. The net effects are a *narrowing* of the jet stream and a deformation of the curvature of the tropopause, which we theorize may be dynamically unstable as a narrower jet can affect barotropic instability (James 1987). As a consequence, both flanks prefer to move in the same direction with the latitudinal span of the jet little changed, thus leading to a deviation from the linear sum.

## 7. Concluding Remarks

Maximum aerosol forcing is centered over the NH low and mid-latitudes. During the boreal winter, the strong local aerosol forcing influences many of the key characteristics of the vigorous extratropical circulation by causing local cooling mainly over the source regions. Such a cooling enhances the meridional temperature gradient equatorward of the NH subtropical jet, but weakens it poleward. The end result is an equatorward shift of the jet.

The cooling over the North Atlantic is much more diffuse than over the North Pacific de-  
 spite similar local forcings. A series of idealized model experiments show that the stationary  
 Rossby waves excited by the anomalous diabatic heating over the tropical East Pacific, when  
 propagating into the NH mid-latitudes, cause a strong trough over the North Pacific. The  
 low pressure anomaly results in a southeastward displacement of the Aleutian low, which is  
 accompanied by an equatorward movement in the time-mean location of the North Pacific  
 subtropical jet and storm track. The associated acceleration of westerlies on the equatorward  
 flank of the jet and deceleration on the poleward flank are consistent with the concentrated  
 cooling over the North Pacific according to the thermal wind relationship. The impacts of the  
 heating anomalies over the tropical Indian Ocean and West Pacific and over the extratropi-  
 cal North Pacific and North Atlantic are secondary. This is consistent with the observation  
 that the tropical Pacific warming and the mid-latitude circulation changes are both El Niño-  
 like in the simulations. The overall pattern of decreased precipitation north of the equator  
 and increased precipitation south is robust across models (Williams et al. 2001; Rotstayn  
 and Lohmann 2002; Feichter et al. 2004; Krisjansson et al. 2005; Ming and Ramaswamy  
 2009). However, the regional response over a specific ocean may be less so. This shows  
 the importance of understanding the detailed spatial pattern of the aerosol-induced tropical  
 circulation change, which plays a critical role in determining the extratropical response by  
 altering stationary Rossby waves.

One can understand the change in atmospheric energy transport by recognizing a few  
 key attributes. A net energy influx into the NH low and mid-latitudes acts to alleviate local  
 aerosol cooling. The zonal-mean meridional latent heat transport is firmly controlled by  
 the thermodynamic scaling in the NH extratropics, even in the presence of large circulation

changes caused by aerosols. This implies that one can predict reliably the changes in zonal-mean precipitation from the global-mean temperature change driven by aerosols and gases without a detailed knowledge of the concurrent circulation changes. On the other hand, the aerosol-induced zonally asymmetrical circulation changes are key to understanding the regional variations in precipitation.

We conclude by emphasizing the fact that the results presented in this paper are based on the simulations performed with a single climate model. It remains to be seen whether the detailed circulation changes discussed here are robust across different models.

#### *Acknowledgments.*

We thank Isaac Held and Gabriel Lau for insightful comments on the manuscript, and Peter Phillips for help with setting up the spectral dynamical core.

## APPENDIX

### Description of Idealized Model Experiments

The atmospheric model is a standard hydrostatic spectral dynamical core forced with the boreal winter diabatic heating derived from the full GCM simulations (namely CONT and BOTH). The vertical differencing follows Simmons and Burridge (1981). Time-stepping is realized with a semi-implicit leapfrog scheme with a Robert-Asselin time filter. The model is run with a horizontal resolution of T42 and 20 evenly spaced  $\sigma$ -layers. The three-dimensional diabatic heating is computed from the GCM simulations described in the main text. The zonal-mean winds and temperature are nudged toward the GCM-simulated boreal winter ones with a timescale of 3 and 15 days, respectively, following the approaches described in (Held and Suarez 1994). For each experiment, the model is integrated for 2000 days, and the last 1000 days are analyzed.

This idealized model differs from the nonlinear stationary wave model used in Held et al. (2002) in a few key aspects. It does not explicitly consider topography, which, though known to be a source of stationary Rossby waves, is not the focus of the current study. As the damping of transients is much weaker than in Held et al. (2002), baroclinic eddies are of comparable strength to those in the full GCM simulations, and act to affect the stationary wave pattern (e.g., Hoerling and Ting 1994). The presence of transient eddies also makes it necessary to average over a longer time period. The zonally asymmetrical diabatic heating

410 controls regional baroclinicity and thus the locations of storm tracks (e.g., Hoskins and  
411 Valdes 1990).

## REFERENCES

- 414 Alexander, M. A., I. Blade, M. Newman, J. R. Lanzante, N. C. Lau, and J. D. Scott, 2002:  
 415 The atmospheric bridge: the influence of ENSO teleconnections on air-sea interaction over  
 416 the global oceans. *J. Climate*, **15**, 2205–2231.
- 417 Chen, G. and I. M. Held, 2007: Phase speed spectra and the recent poleward shift of Southern  
 418 Hemisphere surface westerlies. *Geophys. Res. Lett.*, **34**, doi:doi:10.1029/2007GL031200.
- 419 Chen, G., J. Lu, and D. M. W. Frierson, 2008: Phase speed spectra and the latitude of surface  
 420 westerlies: interannual variability and global warming trend. *J. Climate*, **21**, 5942–5959.
- 421 Feichter, J., E. Roeckner, U. Lohmann, and B. Liepert, 2004: Nonlinear aspects of the  
 422 climate response to greenhouse gas and aerosol forcing. *J. Climate*, **17**, 2384–2398.
- 423 Fischer-Bruns, I., D. F. Banse, and J. Feichter, 2009: Future impact of anthropogenic sulfate  
 424 aerosol on North Atlantic climate. *Climate Dyn.*, **32**, 511–524.
- 425 Forster, P., et al., 2007: Changes in atmospheric constituents and in radiative forcing. *Cli-*  
 426 *mate Change 2007: The Physical Science Basis. Contribution of Working Group I to the*  
 427 *Fourth Assessment Report of the Intergovernmental Panel on Climate Change*, S. Solomon,  
 428 D. Qin, M. Manning, Z. Chen, M. Marquis, K. B. Averyt, M. Tignor, and H. L. Miller,  
 429 Eds., Cambridge University Press, Cambridge, United Kingdom and New York, NY, USA.
- 430 Frierson, D. M. W., J. Lu, and G. Chen, 2007: Width of the Hadley cell in simple and compre-  
 431 hensive general circulation models. *Geophys. Res. Lett.*, **34**, doi:10.1029/2007GL031115.

432 Fu, Q., C. M. Johanson, J. M. Wallace, and T. Reichler, 2006: Enhanced mid-latitude  
433 tropospheric warming in satellite measurements. *Science*, **312**, 1179.

434 Hall, N. M. J., B. J. Hoskins, P. J. Valdes, and C. A. Senior, 1994: Storm tracks in a high-  
435 resolution GCM with doubled carbon dioxide. *Q. J. R. Meteorol. Soc.*, **120**, 1209–1230.

436 Hansen, J., et al., 2005: Efficacy of climate forcings. *J. Geophys. Res.*, **110**, doi:10.1029/  
437 2005JD005776.

438 Haywood, J. M., L. J. Donner, A. Jones, and J.-C. Golaz, 2009: Global indirect radiative  
439 forcing caused by aerosols: IPCC (2007) and beyond. *Clouds in the Perturbed Climate*  
440 *System*, J. Heintzenberg and R. Charlson, Eds., MIT Press, Cambridge, MA, USA.

441 Haywood, J. M., V. Ramaswamy, and B. J. Soden, 1999: Tropospheric aerosol climate  
442 forcing in clear-sky satellite observations over the oceans. *Science*, **283**, 1299–1303.

443 Held, I. M. and B. J. Soden, 2006: Robust responses of the hydrological cycle to global  
444 warming. *J. Climate*, **19**, 5686–5699.

445 Held, I. M. and M. J. Suarez, 1994: A proposal for the intercomparison of the dynamical  
446 cores of atmospheric general circulation models. *Bull. Am. Meteorol. Soc.*, **75**, 1825–1830.

447 Held, I. M., M. Ting, and H. Wang, 2002: Northern winter stationary waves: theory and  
448 modeling. *J. Climate.*, **15**, 2125–2144.

449 Hoerling, M. P. and M. Ting, 1994: Organization of extratropical transients during El Niño.  
450 *J. Climate*, **7**, 745–766.

- Horowitz, L. W., 2006: Past, present, and future concentrations of tropospheric ozone and aerosols: Methodology, ozone evaluation, and sensitivity to aerosol wet removal. *J. Geophys. Res.*, **111**, doi:10.1029/2005JD006937.
- Hoskins, B. J. and P. J. Valdes, 1990: On the existence of storm tracks. *J. Atmos. Sci.*, **47**, 1854–1864.
- Hu, Y. Y. and Q. Fu, 2007: Observed poleward expansion of the hadley circulation since 1979. *Atmos. Chem. Phys.*, **7**, 5229–5236.
- James, I. N., 1987: Suppression of baroclinic instability in horizontally sheared flows. *J. Atmos. Sci.*, **44**, 3710–3720.
- Johanson, C. M. and Q. Fu, 2009: Hadley cell widening: model simulations versus observations. *J. Climate*, **22**, 2713–2725.
- Krisjánsson, J. E., T. Iversen, A. Kirkevåg, O. Seland, and J. Debernard, 2005: Response of the climate system to aerosol direct and indirect forcing: Role of cloud feedbacks. *J. Geophys. Res.*, **110**, doi:10.1029/2005JD006299.
- Kushner, P. J., I. M. Held, and T. L. Delworth, 2001: Southern Hemisphere atmospheric circulation response to global warming. *J. Climate*, **14**, 2238–2249.
- Lau, N. C., 1997: Interactions between global SST anomalies and the midlatitude atmospheric circulation. *B. Am. Meteorol. Soc.*, **78**, 21–33.
- Lindzen, R. S. and B. Farrell, 1980: A simple approximate result for the maximum growth rate of baroclinic instabilities. *J. Atmos. Sci.*, **37**, 1648–1654.



471 Lorenz, D. J. and E. T. DeWeaver, 2007: The tropopause height and the zonal wind response  
 472 to global warming in the IPCC scenario integrations. *J. Geophys. Res.*, **112**, doi:10.1029/  
 473 2006JD008087.

474 Lu, J., G. Chen, and D. M. Frierson, 2008: Response of the zonal mean atmospheric circu-  
 475 lation to El Niño versus global warming. *J. Climate*, **21**, 5835–5851.

476 Lu, J., G. A. Vecchi, and T. Reichler, 2007: Expansion of the Hadley cell under global  
 477 warming. *Geophys. Res. Lett.*, **34**, doi:10.1029/2006GL028443.

478 Manabe, S. and R. T. Wetherald, 1975: The effect of doubling CO<sub>2</sub> concentration on the  
 479 climate of the general circulation model. *J. Atmos. Sci.*, **32**, 3–15.

480 Ming, Y. and V. Ramaswamy, 2009: Nonlinear climate and hydrological responses to aerosol  
 481 effects. *J. Climate*, **22**, 1329–1339.

482 Ming, Y. and V. Ramaswamy, 2011: A model investigation of aerosol-induced changes in  
 483 tropical circulation. *J. Climate*, In press.

484 Ming, Y., V. Ramaswamy, and M. A. Bollasina, 2011a: A model investigation of aerosol-  
 485 induced changes in monsoon circulation. *J. Climate*, in preparation.

486 Ming, Y., V. Ramaswamy, L. J. Donner, and V. T. J. Phillips, 2006: A new parameterization  
 487 of cloud droplet activation applicable to general circulation models. *J. Atmos. Sci.*, **63**,  
 488 1348–1356.

489 Ming, Y., V. Ramaswamy, L. J. Donner, V. T. J. Phillips, S. A. Klein, P. A. Ginoux, ,  
 490 and L. W. Horowitz, 2007: Modeling the interactions between aerosols and liquid water

clouds with a self-consistent cloud scheme in a general circulation model. *J. Atmos. Sci.*,  
**64**, 1189–1209.

Reichler, T., M. Dameris, and R. Sausen, 2003: Determination of tropopause height from  
gridded data. *Geophys. Res. Lett.*, **30**, doi:10.1029/2003GL018240.

Rotstayn, L. D. and U. Lohmann, 2002: Tropical rainfall trends and the indirect aerosol  
effect. *J. Climate*, **15**, 2103–2116.

Simmons, A. J. and D. M. Burridge, 1981: An energy and angular-momentum conserving  
vertical finite-difference scheme and hybrid vertical coordinates. *Mon. Wea. Rev.*, **109**,  
758–766.

The GFDL Global Atmospheric Model Development Team, 2004: The new GFDL global  
atmosphere and land model AM2-LM2: Evaluation with prescribed SST simulations. *J.*  
*Climate*, **17**, 4641–4673.

Toggweiler, J. R., J. L. Russell, and S. R. Carson, 2006: Midlatitude westerlies, at-  
mospheric CO<sub>2</sub>, and climate change during the ice ages. *Paleoceanography*, **21**, doi:  
10.1029/2005PA001154.

Vecchi, G. A., A. Clement, and B. J. Soden, 2008: Examining the Tropical Pacific’s response  
to global warming. *EOS*, **89**, 81–83.

Williams, G. P. and K. Bryan, 2006: Ice age winds: An aquaplanet model. *J. Climate*, **19**,  
1706–1715.

Williams, K. D., A. Jones, D. L. Roberts, C. A. Senior, and M. J. Woodage, 2001: The

511 response of the climate system to the indirect effects of anthropogenic sulfate aerosol.  
512 *Climate Dyn.*, **17**, 845–856.

513 World Meteorological Organization (WMO), 1957: Meteorology A Three-Dimensional Sci-  
514 ence: Second Session of the Commission for Aerology. WMO Bulletin IV(4), WMO,  
515 Geneva.

516 Yin, J. H., 2005: A consistent poleward shift of the storm tracks in simulations of 21st  
517 century climate. *Geophys. Res. Lett.*, **32**, doi:10.1029/2005GL023684.

518 **List of Tables**

519	1	Mean differences in $u_z$ and $\theta_z$ between 10 - 35°N.	28
-----	---	---	----

TABLE 1. Mean differences in  $u_z$  and  $\theta_z$  between 10 - 35°N.

	$\delta u_z$ (m s <sup>-1</sup> )	$\delta \theta_z$ (K)	$\delta u_z/u_z$ (%)	$\delta \theta_z/\theta_z$ (%)	$\delta C/C$ (%)
AERO	1.2	-0.63	8.3	-2.7	11.0
GAS	-0.27	2.08	-1.9	7.8	-9.7
BOTH	1.5	1.1	10.6	4.5	6.1
AERO+GAS	0.92	1.4	3.2	2.8	0.4

## List of Figures

- 1 Radiative flux perturbation of anthropogenic aerosols ( $\text{W m}^{-2}$ ) (colored shading with statistical significance at the 95% confidence level). 33
- 2 Differences in zonal-mean  $\theta$  (K) (the perturbation cases minus CONT; colored shading). The contour lines denote the climatological mean in CONT (between 273 and 323 K). The y-axis is pressure (hPa). 34
- 3 Differences in zonal-mean  $u$  ( $\text{m s}^{-1}$ ) (the perturbation cases minus CONT; colored shading; westerlies as positive) at different pressure levels (hPa). The contour lines denote the climatological mean in CONT (between -20 and 30  $\text{m s}^{-1}$ ). The y-axis is pressure (hPa). 35
- 4 Differences in tropopause height (hPa). Negative values indicate higher tropopause, and vice versa. 36
- 5 Differences in  $T_s$  (K) (BOTH minus CONT; colored shading with statistical significance at the 95% confidence level). The contour lines denote the climatological mean in CONT (between 250 and 300 K). 37
- 6 Differences in 300-hPa  $u$  ( $\text{m s}^{-1}$ ) (the perturbation cases minus CONT; colored shading with statistical significance at the 95% confidence level; westerlies as positive). The contour lines denote the climatological mean in CONT (between 0 and 40  $\text{m s}^{-1}$ ). 38

540	7	Differences in SLP (hPa) (BOTH minus CONT; colored shading with statis-	
541		tical significance at the 95% confidence level). The contour lines denote the	
542		climatological mean in CONT (between 1000 and 1024 hPa).	39
543	8	Differences in 500-hPa $Z$ (10 m) (the perturbation cases minus CONT; colored	
544		shading with statistical significance at the 95% confidence level). The contour	
545		lines denote the climatological mean in CONT (10 m) (between 4000 and 4400	
546		m).	40
547	9	Differences in 300-hPa stationary eddy stream function ( $10^6 \text{ m}^2 \text{ s}^{-1}$ ) (the	
548		perturbation cases minus CONT; colored shading; clockwise circulations as	
549		positive). The contour lines denote the climatological mean in CONT ( $10^6$	
550		$\text{m}^2 \text{ s}^{-1}$ ) (between $-1.5 \times 10^7$ and $1.5 \times 10^7 \text{ m}^2 \text{ s}^{-1}$ ).	41
551	10	Differences in $P$ ( $\text{mm day}^{-1}$ ) (the perturbation cases minus CONT; colored	
552		shading with statistical significance at the 95% confidence level). The contour	
553		lines denote the climatological mean in CONT (between 0 and $22 \text{ mm day}^{-1}$ ).	42

554	11	Differences in 300-hPa stationary eddy stream function ( $10^6 \text{ m}^2 \text{ s}^{-1}$ ) (colored shading; clockwise circulations as positive) simulated with the idealized model in response to the differences in diabatic heating between CONT and BOTH (a) over the entire globe, (b) over the tropical Indian Ocean and West Pacific ( $30^\circ\text{S} - 30^\circ\text{N}$ and $0^\circ - 150^\circ\text{E}$ ), (c) over the tropical East Pacific and Atlantic ( $30^\circ\text{S} - 30^\circ\text{N}$ and $150^\circ\text{E} - 0^\circ$ ), and (d) over the extratropical North Pacific and North Atlantic (north of $30^\circ\text{N}$ ). (e) is the linear sum of (b), (c) and (d). The contour lines denote the climatological mean in the control case ( $10^6 \text{ m}^2 \text{ s}^{-1}$ ) (between $-1.5 \times 10^7$ and $1.5 \times 10^7 \text{ m}^2 \text{ s}^{-1}$ ). The grey arrows sketch the directions in which the stationary Rossby waves propagate.	43
564	12	Differences in 300-hPa transient eddy kinetic energy ( $10 \text{ m}^2 \text{ s}^{-2}$ ) (the perturbation cases minus CONT; colored shading with statistical significance at the 95% confidence level). The contour lines denote the climatological mean in CONT ( $10 \text{ m}^2 \text{ s}^{-2}$ ) (between 20 and $400 \text{ m}^2 \text{ s}^{-2}$ ).	44
568	13	Differences in 500-hPa maximum Eady growth rate ( $10^{-1} \text{ day}^{-1}$ ) (the perturbation cases minus CONT; colored shading with statistical significance at the 95% confidence level). The contour lines denote the climatological mean in CONT ( $10^{-1} \text{ day}^{-1}$ ) (between 0.2 and $1.2 \text{ day}^{-1}$ ).	45
572	14	Differences in zonal-mean northward atmospheric energy transport (PW) (a: the perturbation cases minus CONT; b: AERO minus CONT; c: GAS minus CONT).	46
575	15	Differences in zonal-mean northward atmospheric heat transport (PW) (northward as positive).	47



577	16	Differences in zonal-mean surface temperature (K).	48
578	17	Differences in zonal-mean 300-hPa $u$ ( $\text{m s}^{-1}$ ) (westerlies as positive).	49

FIG. 1. Radiative flux perturbation of anthropogenic aerosols ( $\text{W m}^{-2}$ ) (colored shading with statistical significance at the 95% confidence level).

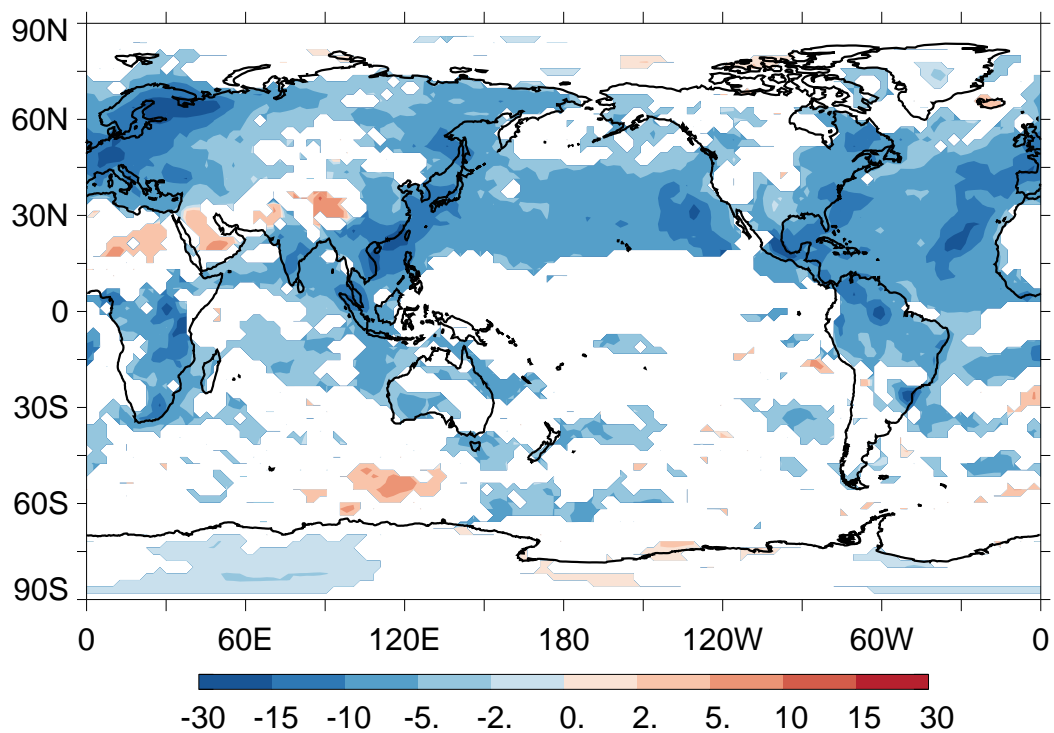


FIG. 2. Differences in zonal-mean  $\theta$  (K) (the perturbation cases minus CONT; colored shading). The contour lines denote the climatological mean in CONT (between 273 and 323 K). The y-axis is pressure (hPa). The y-axis is pressure (hPa). K). The y-axis is pressure (hPa).

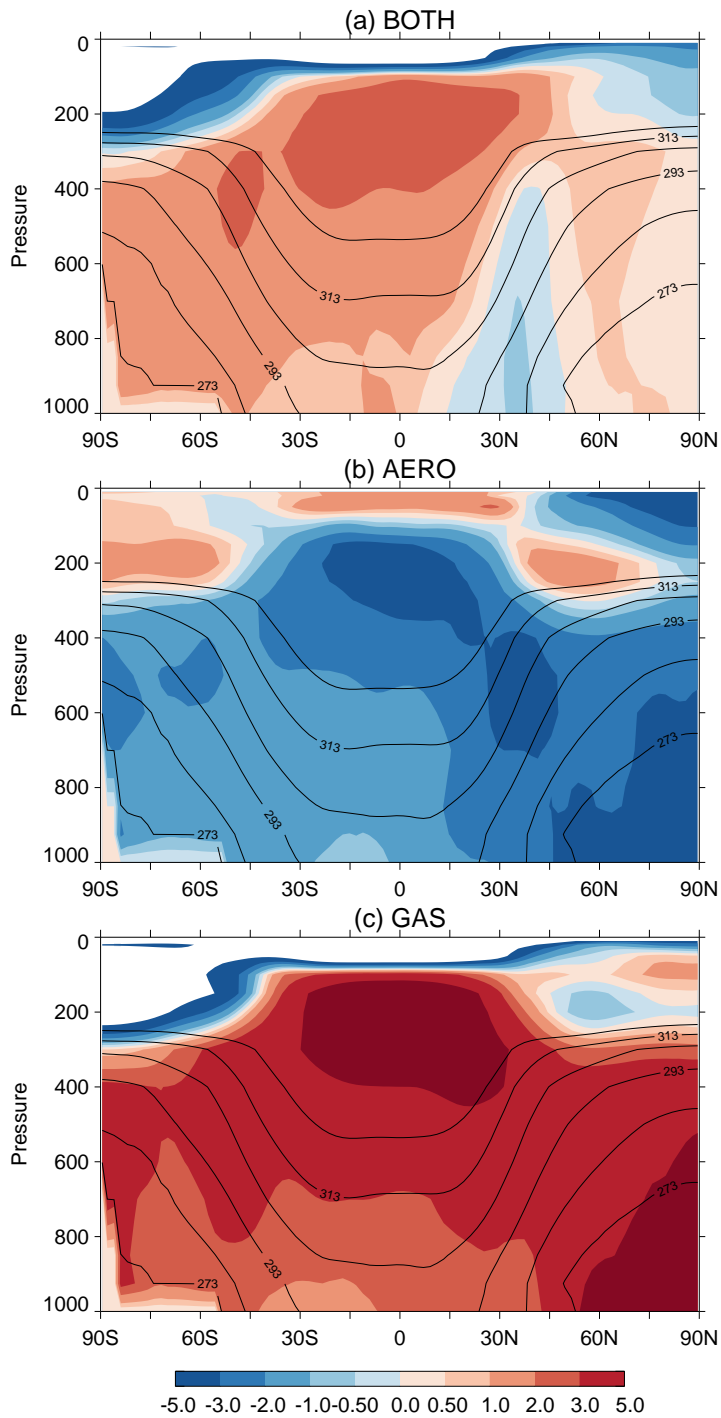


FIG. 3. Differences in zonal-mean  $u$  ( $\text{m s}^{-1}$ ) (the perturbation cases minus CONT; colored shading; westerlies as positive) at different pressure levels (hPa). The contour lines denote the climatological mean in CONT (between  $-20$  and  $30 \text{ m s}^{-1}$ ). The y-axis is pressure (hPa).

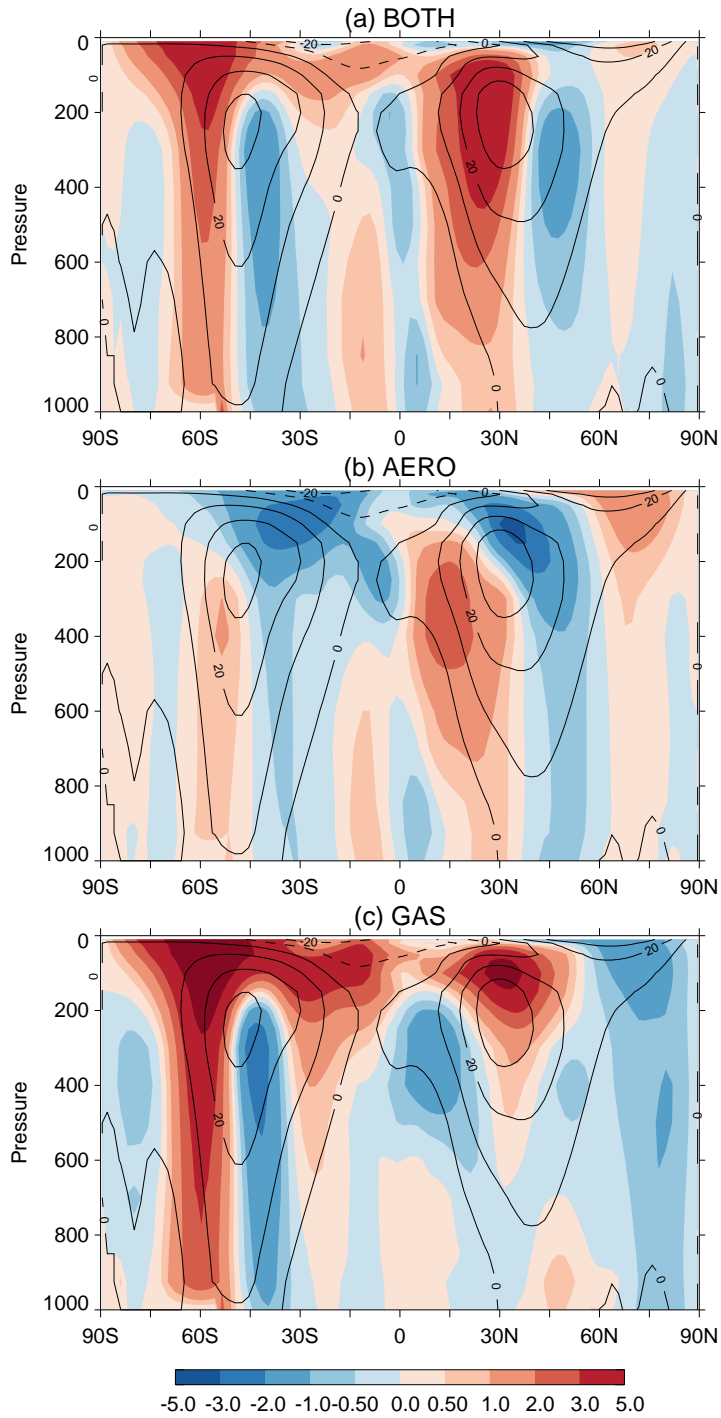


FIG. 4. Differences in tropopause height (hPa). Negative values indicate higher tropopause, and vice versa.

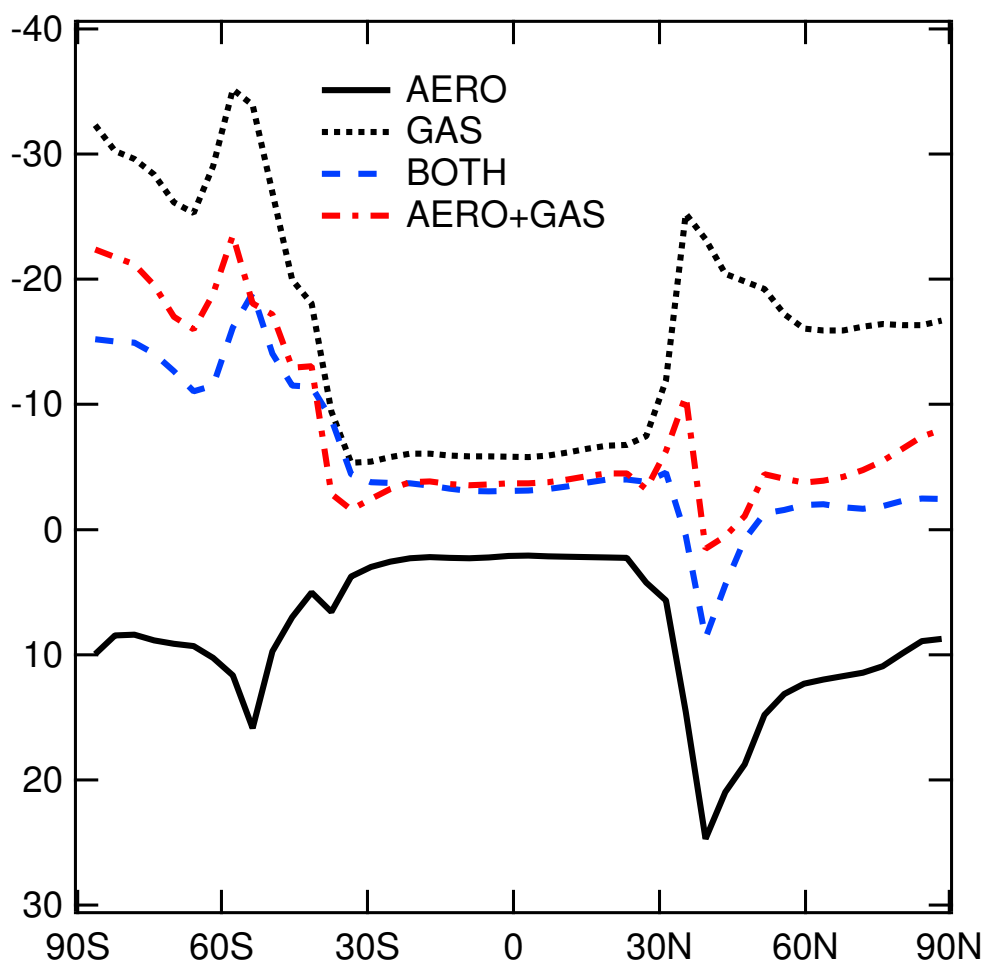


FIG. 5. Differences in  $T_s$  (K) (BOTH minus CONT; colored shading with statistical significance at the 95% confidence level). The contour lines denote the climatological mean in CONT (between 250 and 300 K).

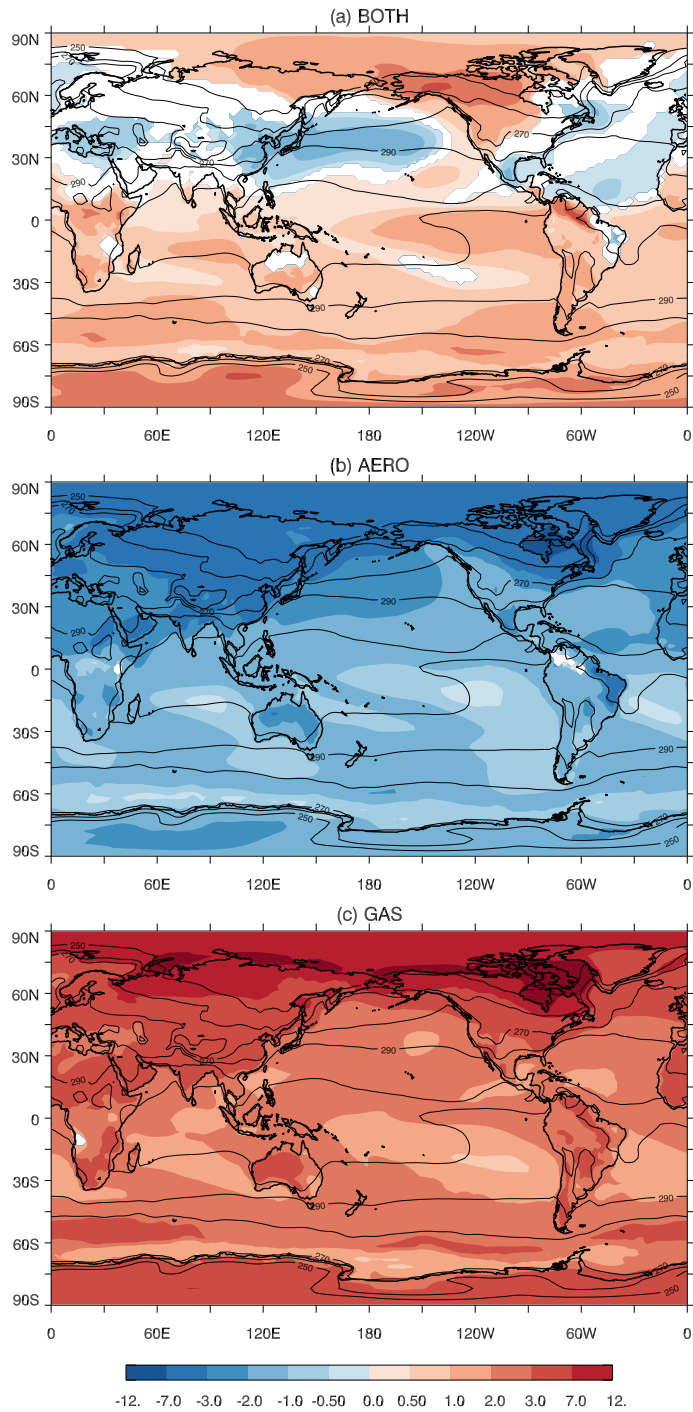


FIG. 6. Differences in 300-hPa  $u$  ( $\text{m s}^{-1}$ ) (the perturbation cases minus CONT; colored shading with statistical significance at the 95% confidence level; westerlies as positive). The contour lines denote the climatological mean in CONT (between 0 and  $40 \text{ m s}^{-1}$ ).

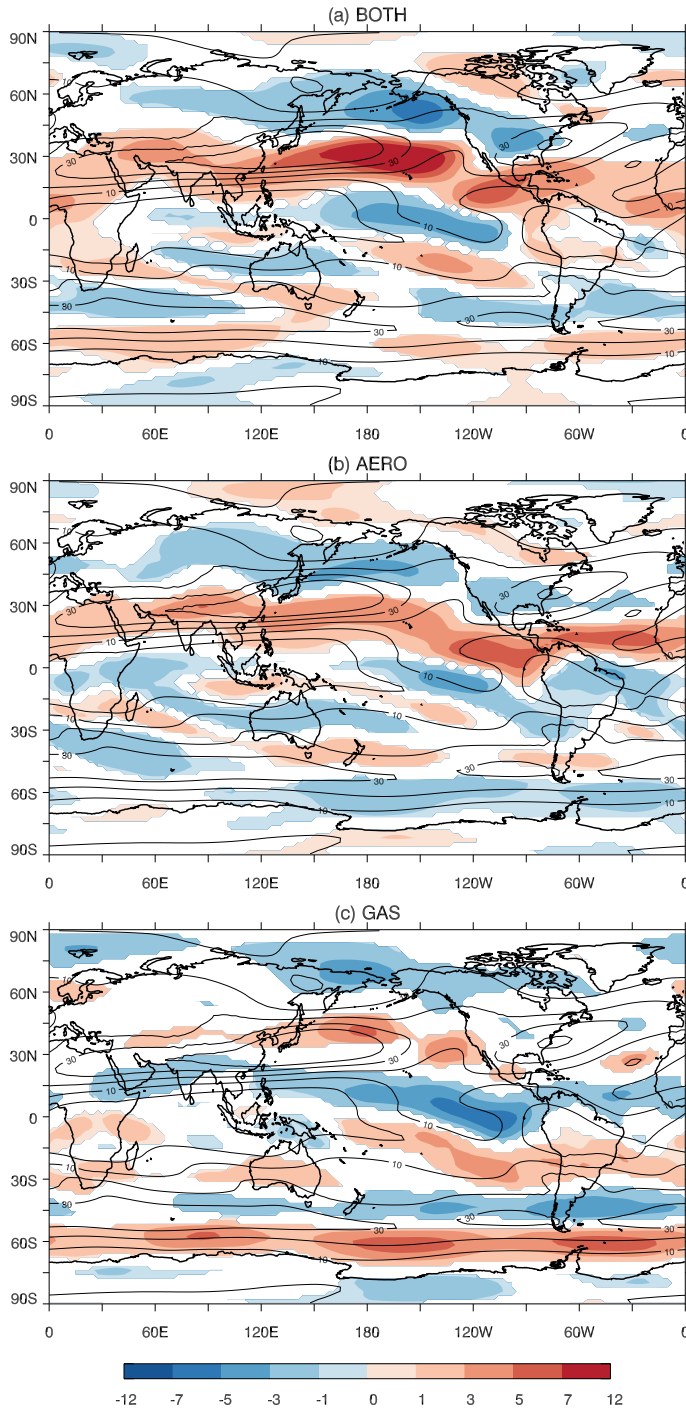


FIG. 7. Differences in SLP (hPa) (BOTH minus CONT; colored shading with statistical significance at the 95% confidence level). The contour lines denote the climatological mean in CONT (between 1000 and 1024 hPa).

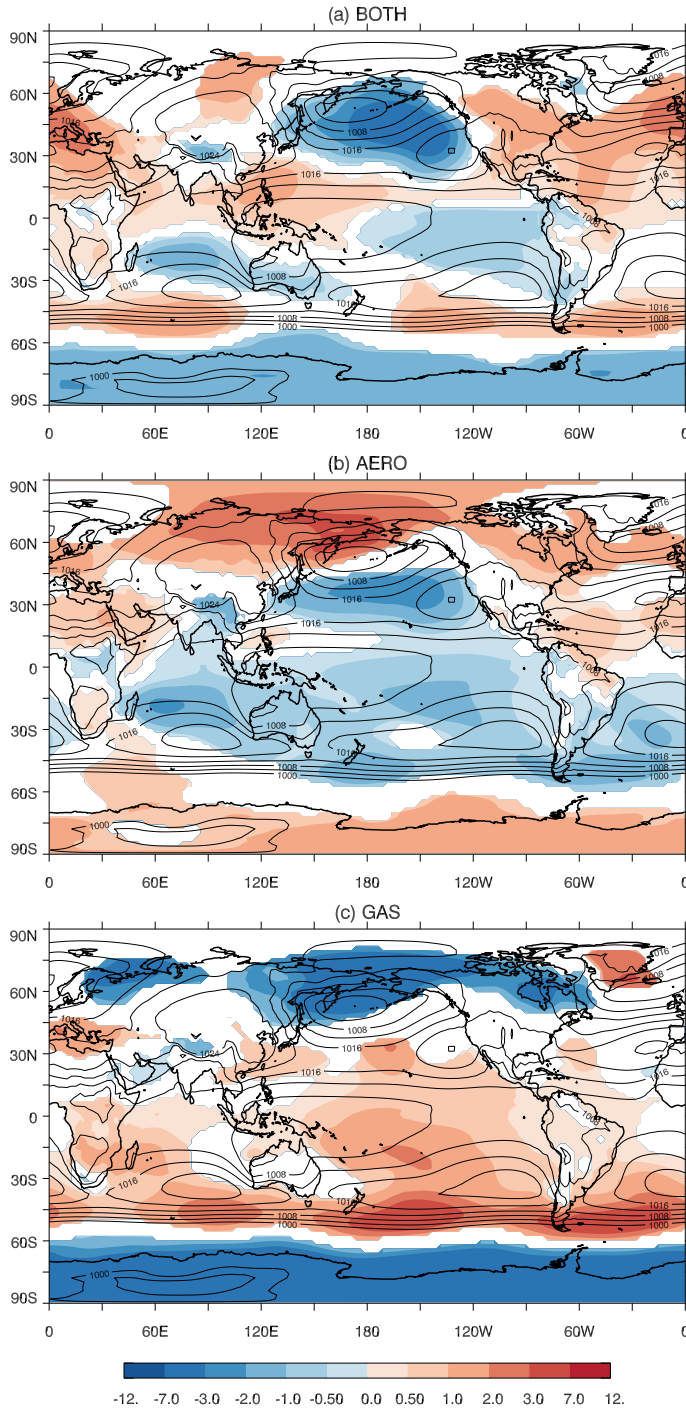




FIG. 8. Differences in 500-hPa  $Z$  (10 m) (the perturbation cases minus CONT; colored shading with statistical significance at the 95% confidence level). The contour lines denote the climatological mean in CONT (10 m) (between 4000 and 4400 m).

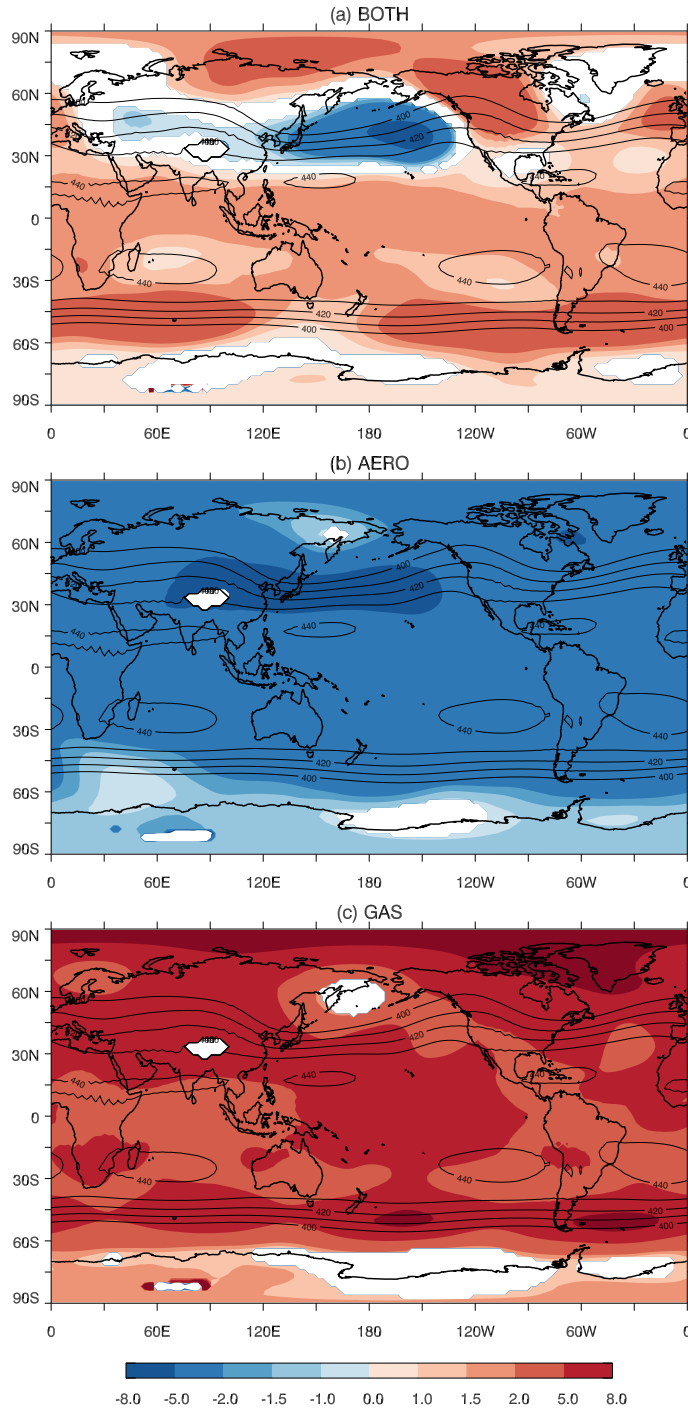


FIG. 9. Differences in 300-hPa stationary eddy stream function ( $10^6 \text{ m}^2 \text{ s}^{-1}$ ) (the perturbation cases minus CONT; colored shading; clockwise circulations as positive). The contour lines denote the climatological mean in CONT ( $10^6 \text{ m}^2 \text{ s}^{-1}$ ) (between  $-1.5 \times 10^7$  and  $1.5 \times 10^7 \text{ m}^2 \text{ s}^{-1}$ ).

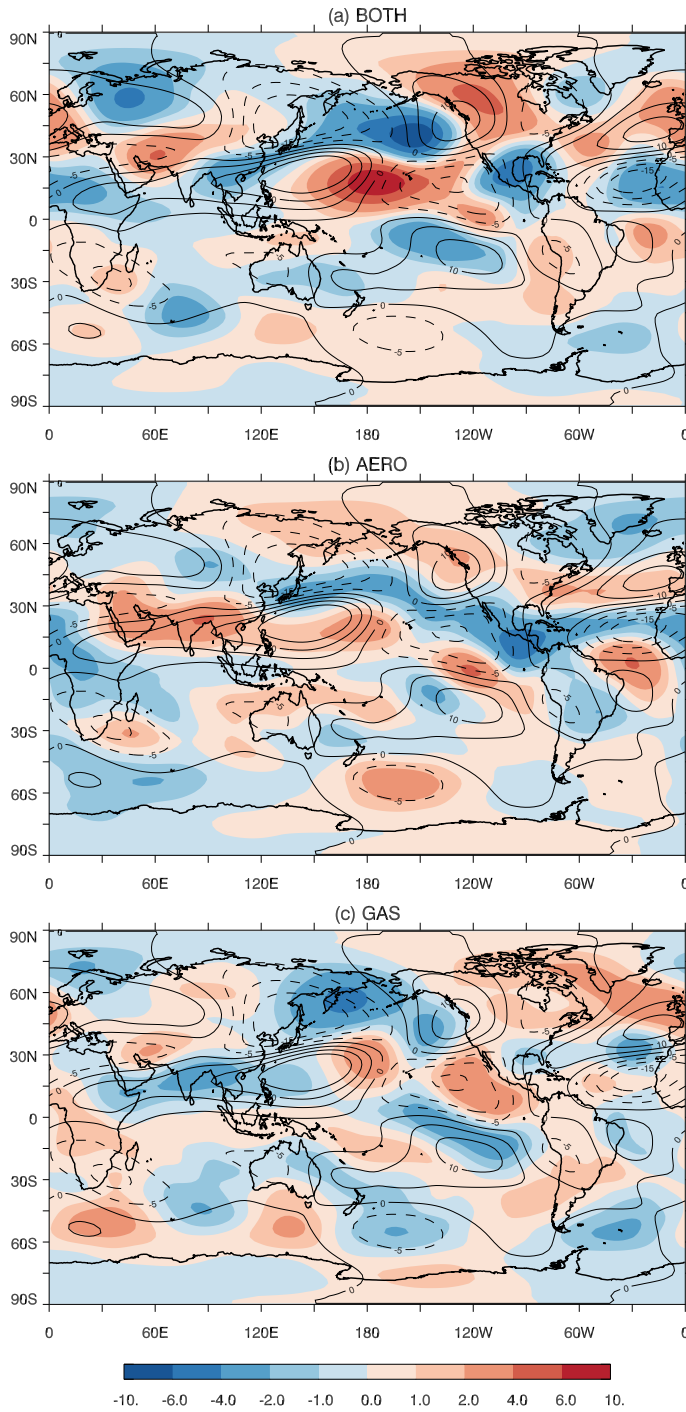


FIG. 10. Differences in  $P$  ( $\text{mm day}^{-1}$ ) (the perturbation cases minus CONT; colored shading with statistical significance at the 95% confidence level). The contour lines denote the climatological mean in CONT (between 0 and 22  $\text{mm day}^{-1}$ ).

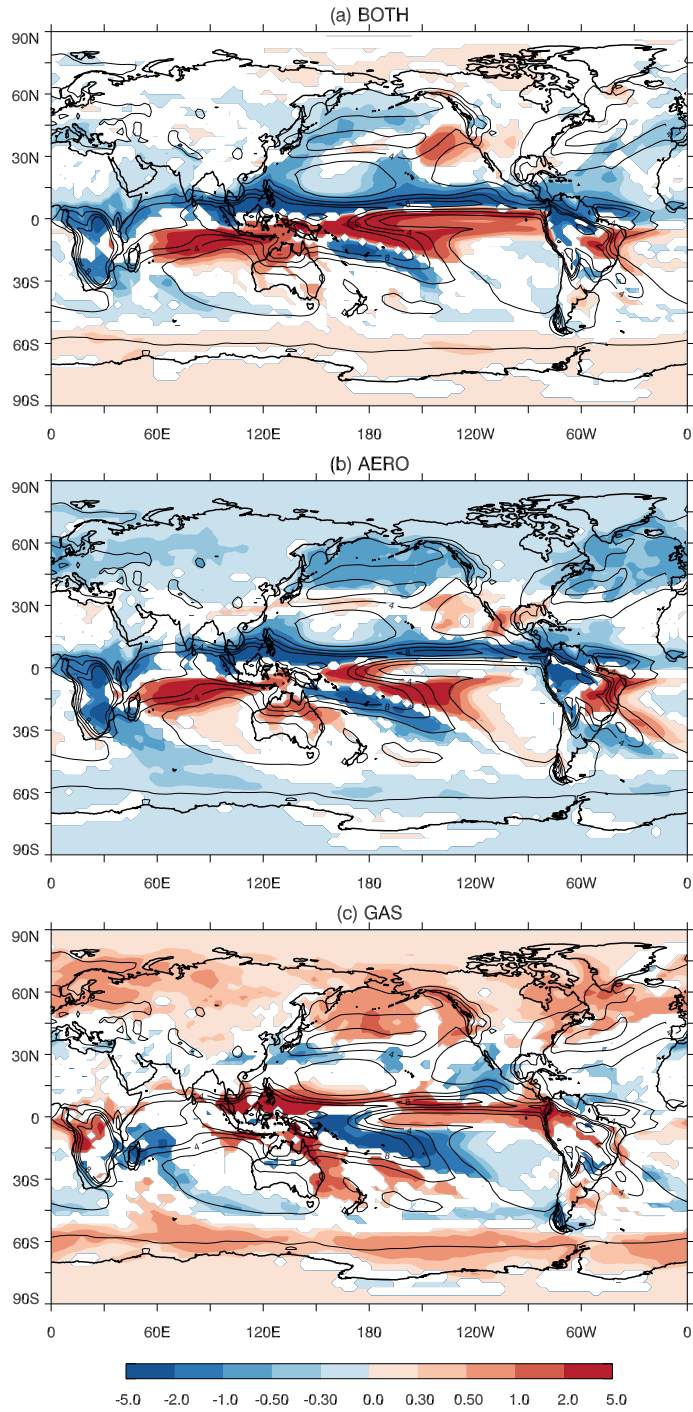


FIG. 11. Differences in 300-hPa stationary eddy stream function ( $10^6 \text{ m}^2 \text{ s}^{-1}$ ) (colored shading; clockwise circulations as positive) simulated with the idealized model in response to the differences in diabatic heating between CONT and BOTH (a) over the entire globe, (b) over the tropical Indian Ocean and West Pacific ( $30^\circ\text{S} - 30^\circ\text{N}$  and  $0^\circ - 150^\circ\text{E}$ ), (c) over the tropical East Pacific and Atlantic ( $30^\circ\text{S} - 30^\circ\text{N}$  and  $150^\circ\text{E} - 0^\circ$ ), and (d) over the extratropical North Pacific and North Atlantic (north of  $30^\circ\text{N}$ ). (e) is the linear sum of (b), (c) and (d). The contour lines denote the climatological mean in the control case ( $10^6 \text{ m}^2 \text{ s}^{-1}$ ) (between  $-1.5 \times 10^7$  and  $1.5 \times 10^7 \text{ m}^2 \text{ s}^{-1}$ ). The grey arrows sketch the directions in which the stationary Rossby waves propagate.

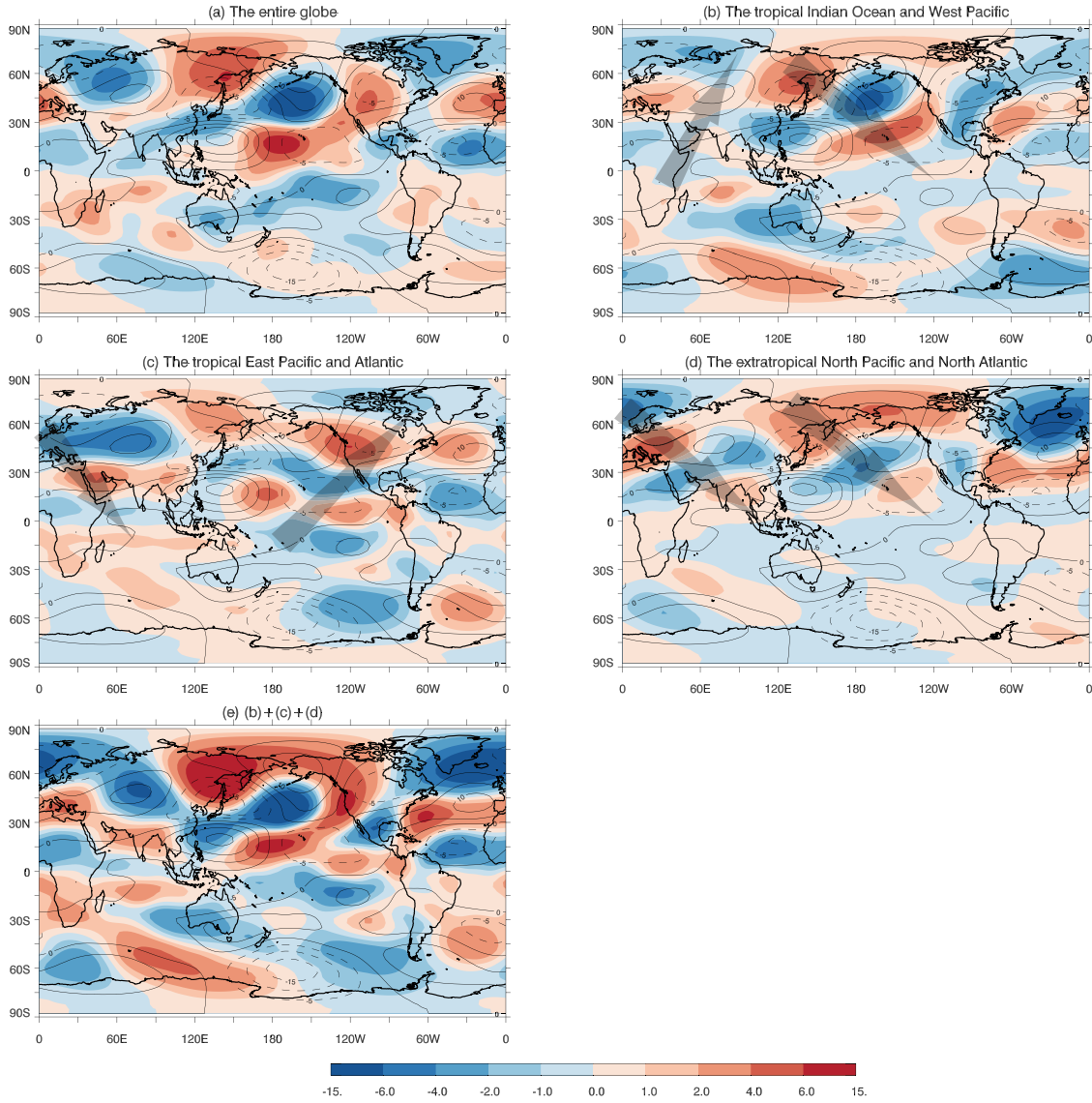


FIG. 12. Differences in 300-hPa transient eddy kinetic energy ( $10 \text{ m}^2 \text{ s}^{-2}$ ) (the perturbation cases minus CONT; colored shading with statistical significance at the 95% confidence level). The contour lines denote the climatological mean in CONT ( $10 \text{ m}^2 \text{ s}^{-2}$ ) (between 20 and  $400 \text{ m}^2 \text{ s}^{-2}$ ).

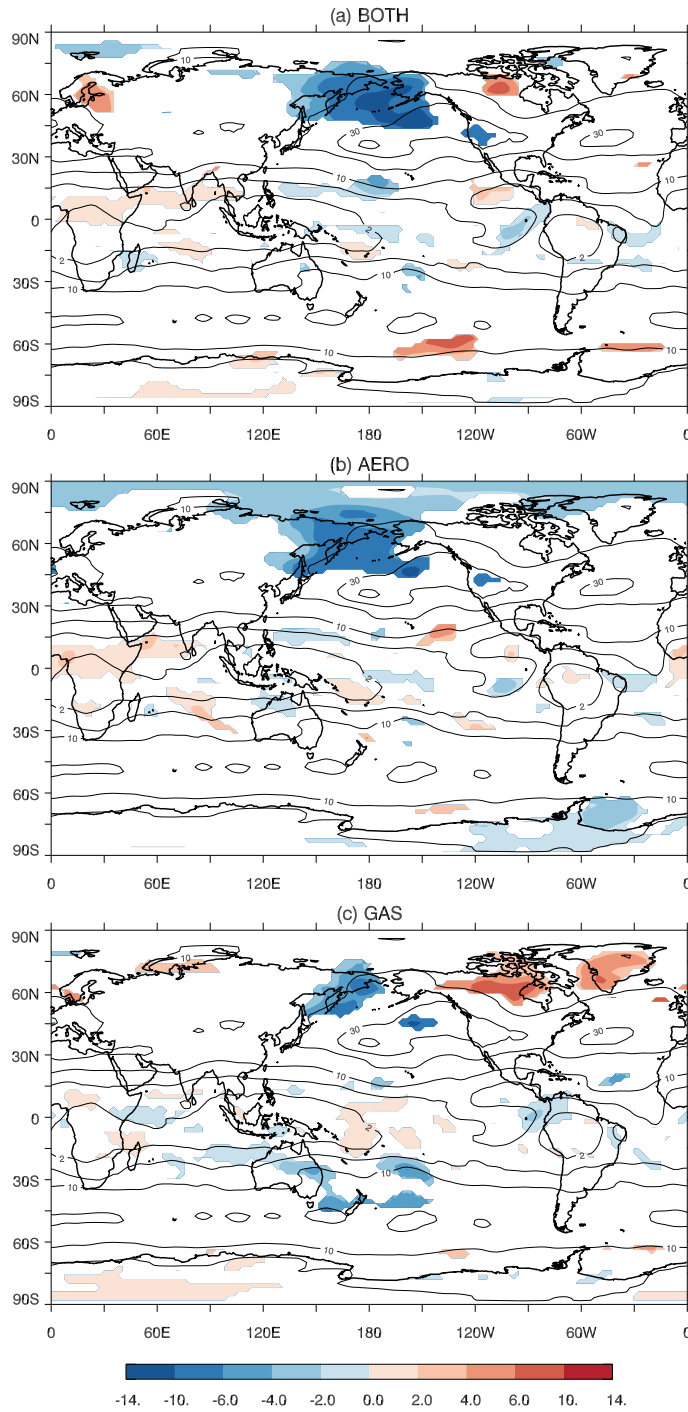




FIG. 13. Differences in 500-hPa maximum Eady growth rate ( $10^{-1} \text{ day}^{-1}$ ) (the perturbation cases minus CONT; colored shading with statistical significance at the 95% confidence level). The contour lines denote the climatological mean in CONT ( $10^{-1} \text{ day}^{-1}$ ) (between 0.2 and  $1.2 \text{ day}^{-1}$ ).

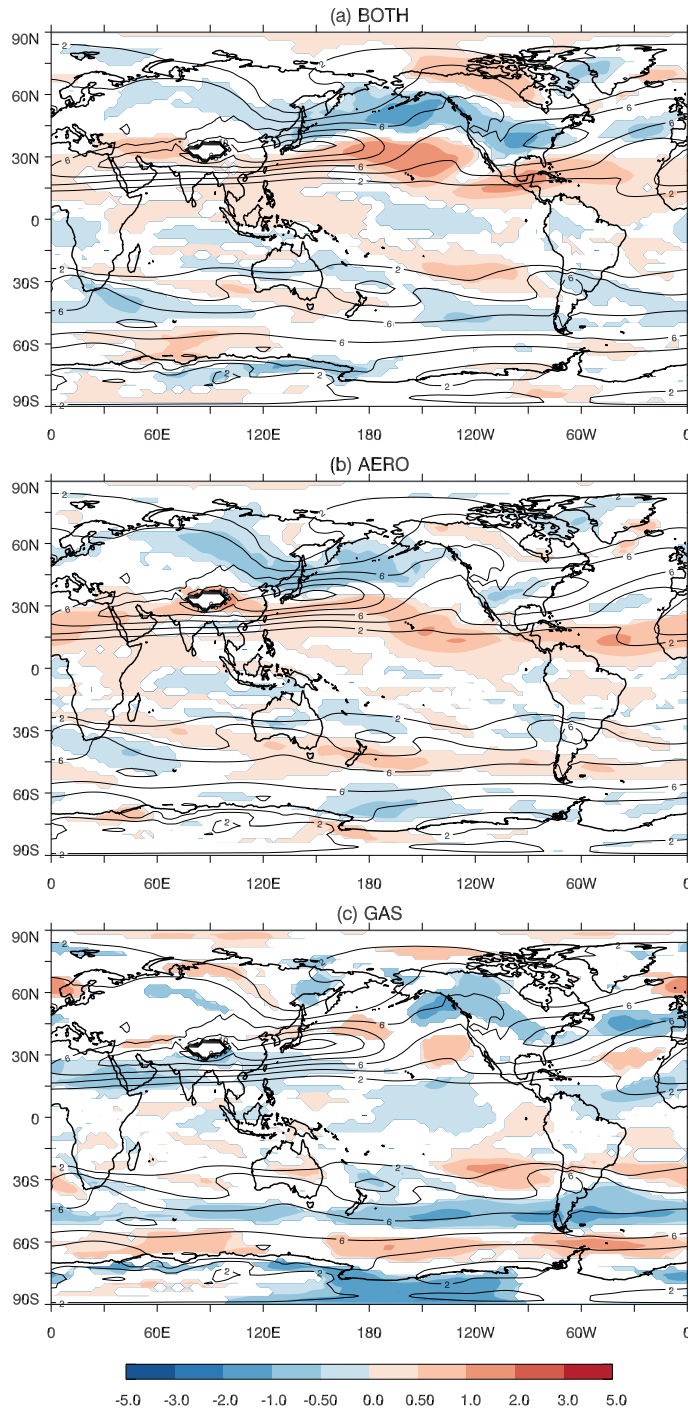


FIG. 14. Differences in zonal-mean northward atmospheric energy transport (PW) (a: the perturbation cases minus CONT; b: AERO minus CONT; c: GAS minus CONT).

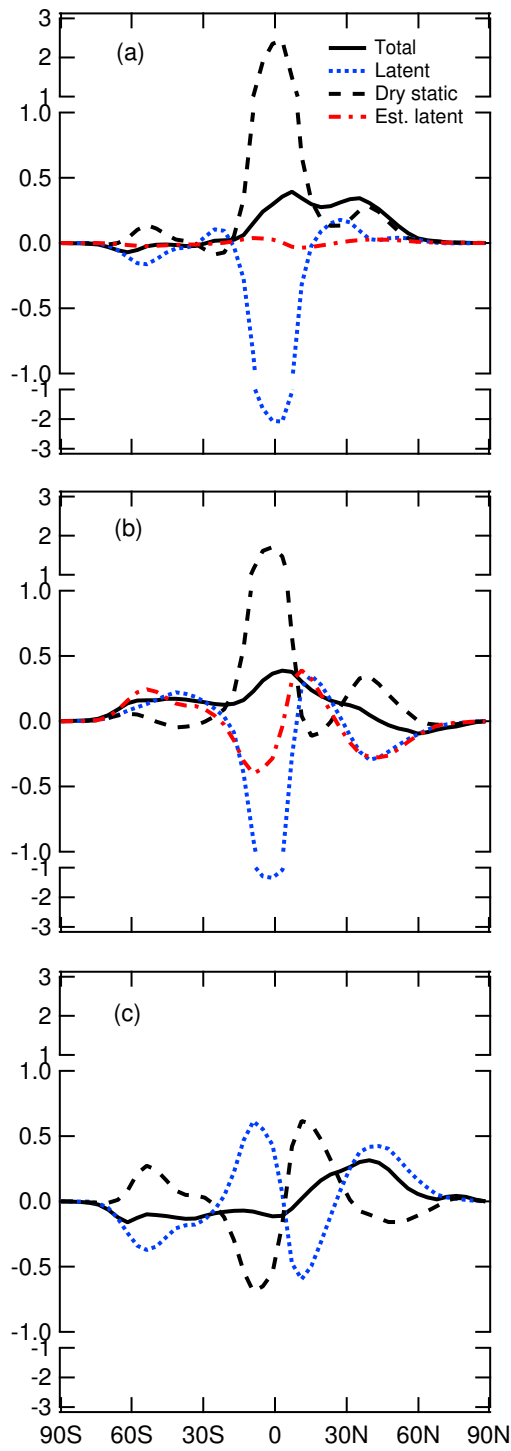


FIG. 15. Differences in zonal-mean northward atmospheric heat transport (PW) (northward as positive).

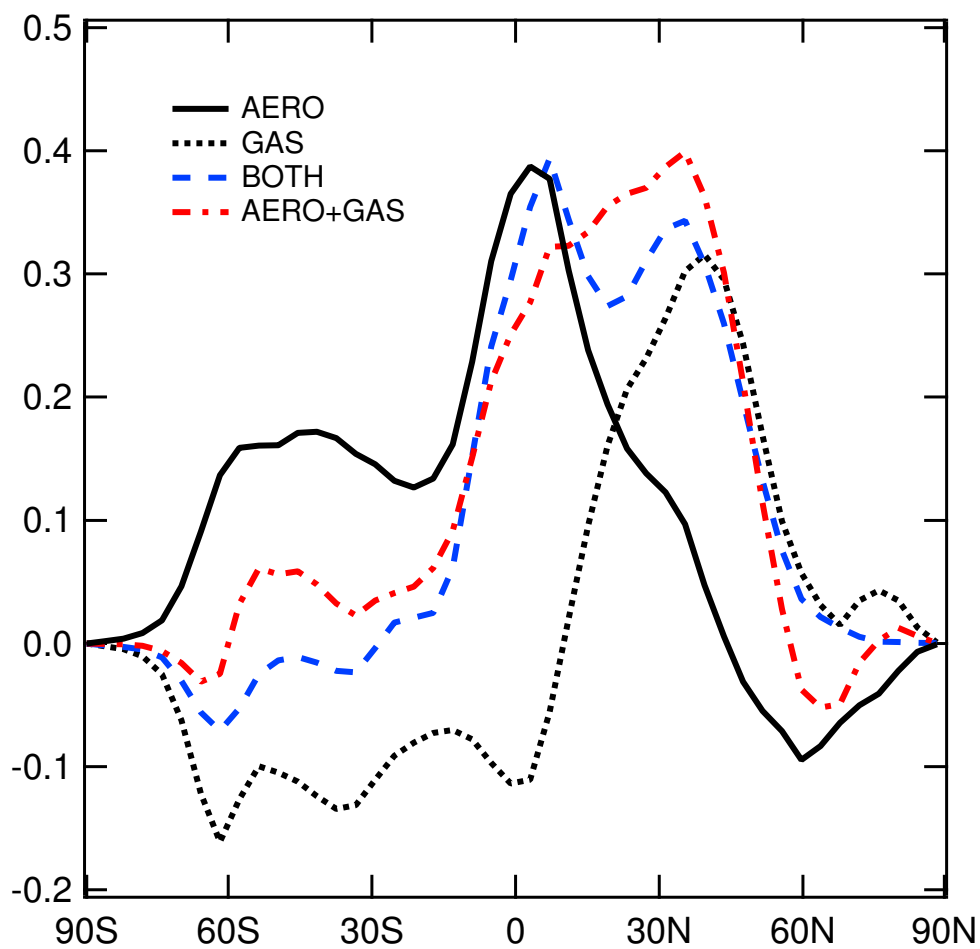




FIG. 16. Differences in zonal-mean surface temperature (K).

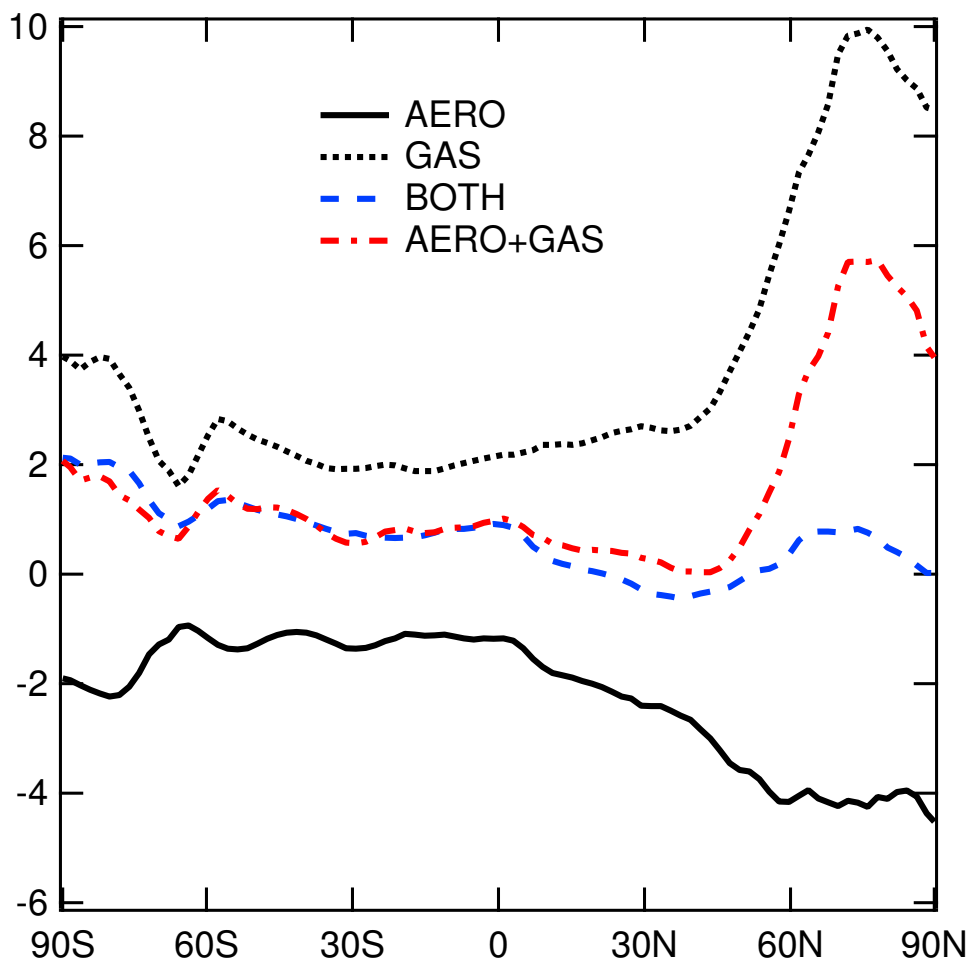


FIG. 17. Differences in zonal-mean 300-hPa  $u$  ( $\text{m s}^{-1}$ ) (westerlies as positive).

